THE JOURNAL OF PHYSICAL CHEMISTRY LETTERS
A JOURNAL OF THE AMERICAN CHEMICAL SOCIETY

pubs.acs.org/JPCL

Letter

Bismuth Doping Alters Structural Phase Transitions in Methylammonium Lead Tribromide Single Crystals

Erin Jedlicka,[⊥] Jian Wang,[⊥] Joshua Mutch, Young-Kwang Jung, Preston Went, Joseph Mohammed, Mark Ziffer, Rajiv Giridharagopal, Aron Walsh, Jiun-Haw Chu, and David S. Ginger*

Cite This: *J. Phys. Chem. Lett.* 2021, 12, 2749–2755

Read Online

ACCESS | Metrics & More | Article Recommendations | Supporting Information

ABSTRACT: We study the effects of bismuth doping on the crystal structure and phase transitions in single crystals of the perovskite semiconductor methylammonium lead tribromide, $MAPbBr_3$. By measuring the temperature-dependent specific heat capacity (C_p), we find that as the Bi doping increases, the phase transition assigned to the cubic to tetragonal phase boundary decreases in temperature. Furthermore, after doping we observe one phase transition between 135 and 155 K, in contrast to two transitions observed in the undoped single crystal. These results appear strikingly similar to previously reported effects of mechanical pressure on perovskite crystal structure. Using X-ray diffraction, we show that the lattice constant decreases as Bi is incorporated into the crystal, as predicted by density functional theory. We propose that bismuth substitutional doping on the lead site is dominant, resulting in Bi_{Pb}^{+} centers that induce compressive chemical strain that alters the crystalline phase transitions.

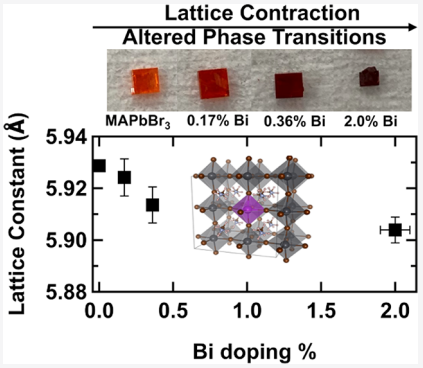

Halide perovskites have emerged as promising semiconductor materials for applications including solar cells, light-emitting diodes, photodetectors, and lasers.[1−4] They exhibit unique and tunable optoelectronic properties via facile tailoring of the chemical composition of the structure. In the archetypal perovskite ABX_3 crystal structure, A represents a monovalent cation species (A = Cs^+, $CH_3NH_3^+$ (MA^+), $(NH_2)_2CH_3^+$ (FA^+)), B represents a divalent cation (B = Pb^{2+}, Sn^{2+}), and X represents a halide (X = Cl^-, Br^-, I^-). Diverse electronic and structural motifs are thereby accessible by modification of the chemical composition and the dimensionality of the material.[5] Doping provides an additional lever for changing the properties of lead halide perovskites by substituting a selected impurity into the crystal at low concentrations. Several dopant species, including Bi^{3+}, Cd^{2+}, K^+, Mn^{2+}, Ce^{3+}, Yb^{3+}, and Eu^{3+},[5−13] have been studied with regard to their effects on the optoelectronic properties of the lead halide perovskites. However, there have been relatively fewer studies of how doping, defects, and impurities affect the structural properties of halide perovskite crystals and nanocrystals. Doping and defects can affect temperature-dependent phase transition behavior and can alter the lattice constant and strain.[13−15] Understanding these phenomena is important for tailoring materials properties and for engineering materials with improved stability in varying operational conditions.

In this work, we study the effects of dopant inclusion on the crystal structure in a series of single crystals of the hybrid organic−inorganic lead halide perovskite methylammonium lead tribromide ($MAPbBr_3$) with various amounts of bismuth doping. We chose this system for several reasons. First, the optoelectronic properties of bismuth-doped perovskites have been well-characterized, among many other dopants, e.g., quenching of visible photoluminescence with corresponding near-infrared (NIR) emission, increasing conductivity, increased free carrier concentrations, and increased carrier lifetimes.[6−10,13,16] Second, recently developed crystallization methods for $MAPbBr_3$ report rapid growth of high-purity macroscopic millimeter-sized single crystals with bismuth doping,[6−10,16−18] which offer an ideal platform to study the intrinsic dopant effects on the crystal structure without the complication of extrinsic influences such as surfaces or grain boundaries.[19] Finally, a number of studies on the crystal structure and phase transitions of undoped $MAPbBr_3$, under both atmospheric conditions and external pressure are available, providing a firm literature basis for further analysis.[20−26]

Here we investigate the effects of Bi doping on the phase transition behavior of $MAPbBr_3$ single crystals using specific heat capacity (C_p) measurements. We show that as the Bi doping level increases, the temperature of the phase transition assigned to the cubic to tetragonal phase of $MAPbBr_3$ decreases. Additionally, upon incorporation of bismuth into the $MAPbBr_3$ crystal lattice, we observe a single phase

Received: February 2, 2021
Accepted: March 9, 2021
Published: March 11, 2021

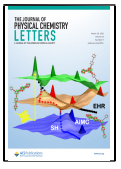

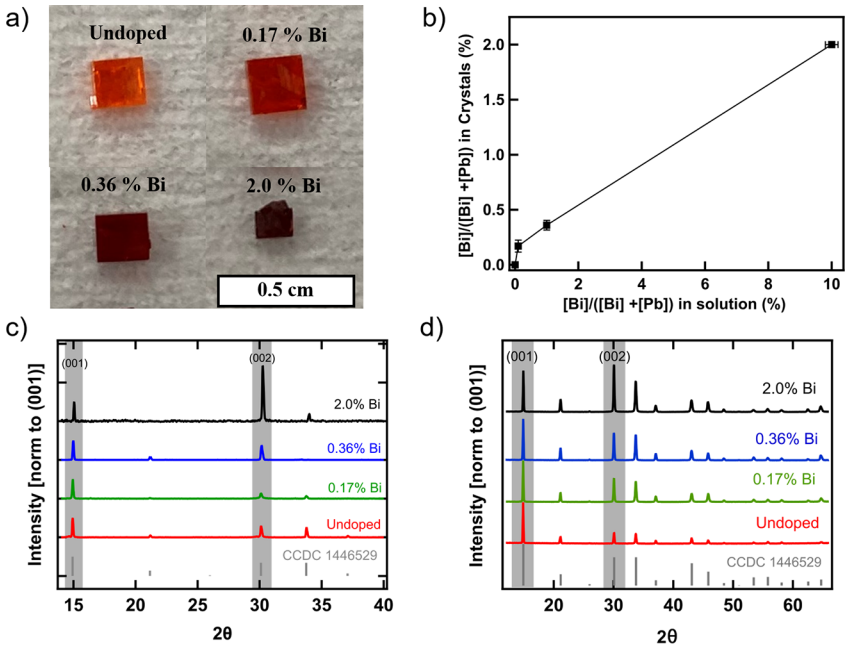

Figure 1. Characterization of $MAPbBr_3$ single crystals with various levels of bismuth doping. (a) $MAPbBr_3$ single crystals. (b) Ratio of Bi to total amount of Pb and Bi in single crystals vs the growth solution. (c) single-crystal X-ray diffraction patterns. (d) Powder X-ray diffraction patterns.

transition between 135 and 155 K instead of the two phase transitions in that temperature range observed in the undoped $MAPbBr_3$ crystal. These changes in phase transition behavior occur alongside a lattice contraction induced by the Bi substitutional doping at the Pb site. We compare the lattice contraction observed in X-ray diffraction (XRD) to first-principles predictions at the various doping levels for both Bi_{Pb}^{0} and Bi_{Pb}^{+} defect sites. We propose that the incorporation of Bi occurs through a Bi_{Pb}^{+} defect site, which induces compressive chemical strain, resulting in a lattice contraction and the changes in the phase transition behavior.

We grow single-crystal $MAPbBr_3$ incorporating various concentrations of bismuth following the inverse temperature crystallization method reported by Nayak and co-workers.[6] Detailed growth methods are provided in the Supporting Information. Figure 1a shows as-prepared $MAPbBr_3$ single crystals with increasing bismuth concentration. As previously reported, we observe that bismuth doping induces strong changes in color for $MAPbBr_3$ single crystals, from translucent orange (undoped) to an increasingly darker red color (from 0.1% to 1% in solution) and then to opaque black at the highest Bi doping (10% in solution) levels.[6−8] This color change has been attributed to an increasing number of sub-band-gap states with increasing Bi doping level.[6]

To quantify the bismuth doping level in our single crystals, which can differ from the amount of Bi added to the growth solution,[6,7] we use inductively coupled plasma optical emission spectrometry (ICP-OES) to determine the ratio of bismuth to lead in our single crystals. Figure 1b shows a plot of the ICP-OES-measured Bi concentration in the final crystal as a function of the Bi concentration in the growth solution. As shown in Figure 1b, we observe increasing bismuth concentration for crystals grown with higher bismuth concentrations in solution and confirm no detectable bismuth concentration in our undoped samples. We report final bismuth concentrations of 0.17%, 0.36%, and 2.0% for the 0.1%, 1%, and 10% bismuth solutions, respectively. In agreement with previous reports, we find that at high concentrations of bismuth in the growth solution, the concentration of bismuth incorporated into the crystal is lower than the concentration of bismuth in the growth solution.[6,7]

Figure 1c,d shows the XRD patterns, intensity-normalized to the (001) plane, for both $MAPbBr_3$ single crystal and crushed powders, respectively. Both sets of XRD data show that the diffraction patterns after Bi doping agree with the undoped $MAPbBr_3$ reference pattern reported by Jaffe and co-workers[27] and are consistent with previous reports.[6−8] We note that the diffraction intensity of the (002) plane increases, with respect to (001), as the bismuth level in the crystal increases. Such an increasing trend in the (002) to (001) intensity with the bismuth-doping level can be found in the XRD patterns in other literature reports,[6−8] though the effect was not discussed or explained. We propose that the observed increase in the (002)/(001) ratio upon Bi doping indicates increasing lattice disorder in the Bi-doped single crystals. Previous studies on undoped crystals have similarly correlated increases in the (002)/(001) intensity ratio with increasing long-range disorder, as verified by far-infrared reflection (FIR) spectroscopy.[28] More ordered $MAPbBr_3$ crystals, those with fewer stacking faults or dislocations as quantified by a higher far-infrared reflectance intensity, also exhibit higher (001) diffraction peak intensities with respect to their (002) planes. This result is also consistent with the optical microscopy images (Figure S1), where we clearly resolve hillock-like crystalline growth fronts in the undoped crystal. We observe fewer such growth fronts on the 0.17% Bi-doped crystal and no such front on the 0.36% and 2.0% Bi-doped crystals, suggesting less long-range order.

Next, to understand the potential impact of the Bi doping on the phase transition behaviors, we perform temperature-dependent specific heat capacity measurements as a function of bismuth doping concentration. Specific heat capacity measurements have been applied to study the temperature-

https://dx.doi.org/10.1021/acs.jpclett.1c00334
J. Phys. Chem. Lett. 2021, 12, 2749−2755

dependent phase transition behaviors of lead halide perovskites, which have been demonstrated to depend both on the A-site alloying (FA, Cs) and X-site halide selection;[20,29] however, the effects of B-site doping and substitution are less explored. Recently, Ma and co-workers showed that replacing Pb^{2+} with Ni^{2+} at the B site in $CsPbCl_3$ nanocrystals alters the local structure of the doped regions and inhibits the cubic to orthorhombic phase transition.[15] Here we expect that heterovalent B-site doping, such as Bi^{3+} on Pb^{2+}, might also alter the phase transition behavior.

Figure 2 shows the heat capacity as measured using a Physical Properties Measurement System (PPMS) Dynacool (Quantum Design) for four $MAPbBr_3$ samples with different Bi doping levels. Additionally, we show a reference C_p versus T plot with phase assignments as reported by Onoda-Yamamuro and co-workers.[20] In Figure 2, the baseline represents the normal part heat capacity as a result of different vibrational modes, whereas the transitional peaks correspond to the $MAPbBr_3$ phase transition temperatures.[20] We observe three phase transitions in our undoped $MAPbBr_3$ crystals, which we determine from where the first derivative of the specific heat capacity equals zero. The peaks we measure for the undoped sample agree well with those measured by Onoda-Yamamuro et al.

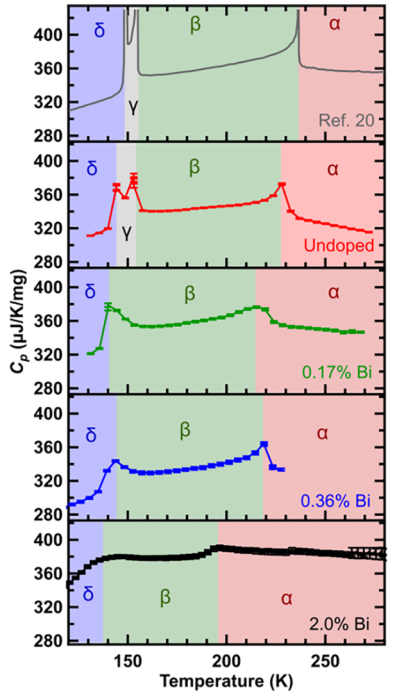

Figure 2. Temperature-dependent specific heat capacity (C_p) for various levels of bismuth doping. Phase transitions are color-coded as follows: red, cubic phase (α); green, tetragonal phase I (β); gray, tetragonal phase II (γ); blue, orthorhombic phase (δ).

Following the previous phase transition assignments,[30,31] we identify them as (1) the transition between α-$MAPbBr_3$ (cubic, $Pm3m$) and β-$MAPbBr_3$ (tetragonal, $I4/mcm$) at 228 K, (2) the transition between β-$MAPbBr_3$ (tetragonal, $I4/mcm$) and γ-$MAPbBr_3$ (tetragonal, $P4/mmm$) at 153 K, and (3) the transition between γ-$MAPbBr_3$ (tetragonal, $P4/mmm$) and δ-$MAPbBr_3$ (orthorhombic, $Pnma$) at 144 K. We assign space groups for the cubic and tetragonal phases according to studies by Poglitsch and Weber.[30] For the low-temperature orthorhombic phase, we follow the assignment from Swainson and co-workers,[31] who suggested that the $Pnma$ space group yields more satisfactory refinement without missing symmetry compared with the previously reported $Pna2_1$ assignment. For the convenience of the reader, we have included the detailed crystal structure information for the different phases of $MAPbBr_3$ in Table S1. After Bi doping, we observe a few additional features: (1) the temperature of the phase transition between the cubic phase (α) and the tetragonal phase (β) shifts to lower temperatures, as shown by the expansion of the cubic phase in Figure 2, represented by the red-shaded region of the plot for the bismuth-doped samples; (2) there is only one low-temperature phase transition between the tetragonal and orthorhombic phases, as shown by the disappearance of the doublet peaks near 150 K, likely indicating the loss of the lower-temperature tetragonal phase (γ);[26] (3) as the doping level increases, the phase transition peaks become less definitive and turn into gradual bumpy transition features. We note that the crystals with the highest doping level (2%) show greater sample-to-sample variations, as can be seen in

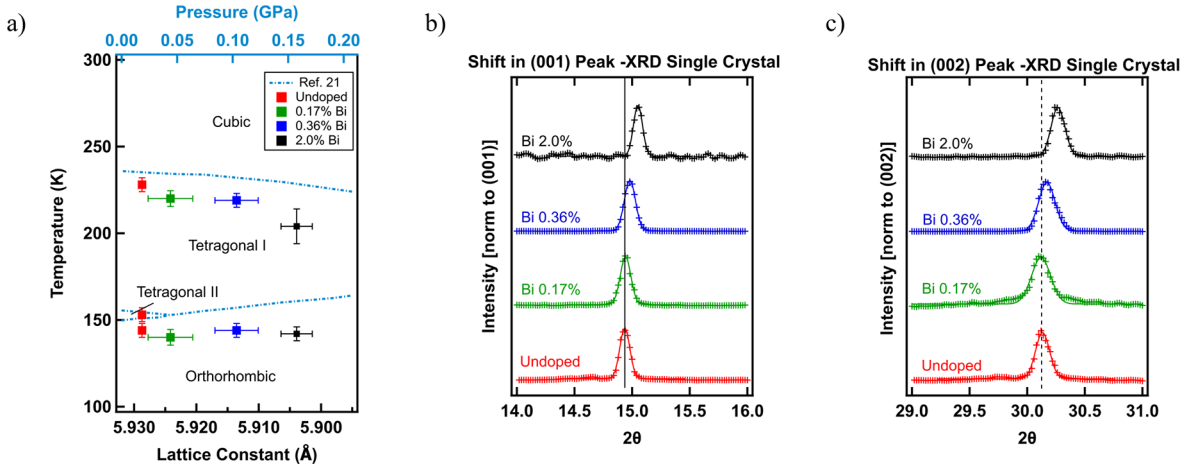

Figure 3. (a) Phase transition temperatures for pure $MAPbBr_3$ as functions of increasing pressure (blue lines, ref 21) and for increasing levels of Bi doping as functions of the lattice spacing. The lattice constant (bottom axis) and pressure (top axis) are registered according to a pressure-dependent $MAPbBr_3$ lattice constant study.[34] (b, c) Single-crystal X-ray diffraction (XRD) patterns showing shifts in the (001) and (002) peaks to higher diffraction angles with increasing Bi doping level.

https://dx.doi.org/10.1021/acs.jpclett.1c00334
J. Phys. Chem. Lett. 2021, 12, 2749−2755

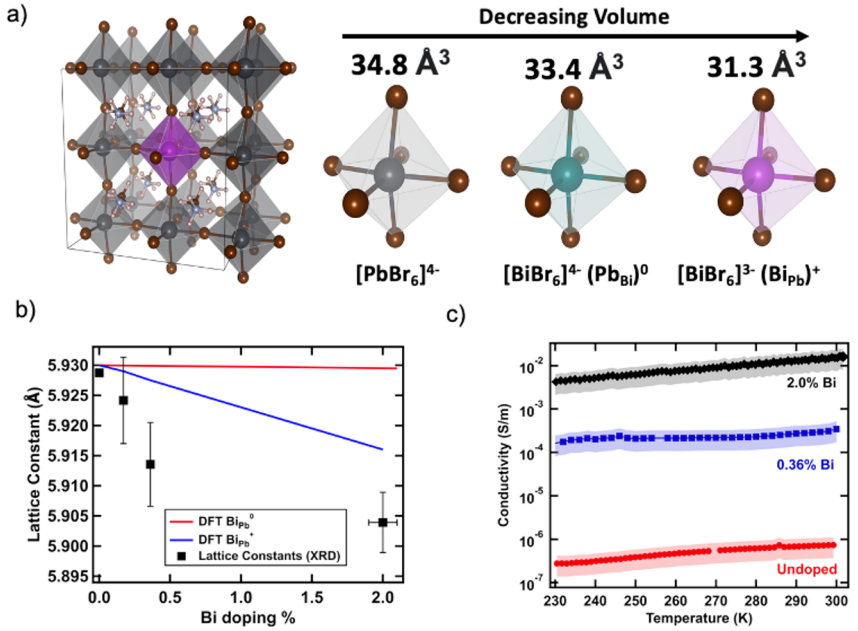

Figure 4. (a) Optimized structure of $MAPbBr_3$ 2 × 2 x 2 super cell geometry of octahedra in $MAPbBr_3$ lattice depending on center ions; (b) Lattice constants determined through DFT calculation (red and blue lines) and XRD (black markers); (c) Temperature-dependent conductivity measurements for single crystals.

Figure S2, but that all follow the above trends qualitatively. We attribute these variations to the wider range of crystallization temperatures we observed for the 2% Bi-doped single crystals. We speculate that the 2.0% Bi single crystals thus have more variation in local crystallinity, which could alter the C_p behavior between samples with the same nominal concentration of bismuth.

To understand the origin and implication of these observations, we compare them with similar behaviors found in the undoped $MAPbBr_3$ single-crystal phase transition under external pressure. Onoda-Yamamuro et al. showed that (Figure 3a, dashed lines with respect to the top axis) for undoped $MAPbBr_3$ single crystals, as the external mechanical pressure increases, (1) the transition between the cubic phase and the tetragonal phase shifts to lower temperatures, and (2) the doublet peaks corresponding to the two tetragonal phases near 150 K disappear.[21] The cause of the pressure-induced behavior is understood to be the unit cell volume reduction due to tilting and shrinking of the $PbBr_6$ octahedra.[32] The presence of two tetragonal phases, $I4/mcm$ (β) at higher temperature and $P4/mmm$ (γ) at lower temperature, is unique to $MAPbBr_3$, contrasting with $MAPbCl_3$ and $MAPbI_3$, each of which has only one tetragonal phase. Onoda-Yamamuro and co-workers mentioned that the lower temperature tetragonal (γ) phase for $MAPbBr_3$ corresponds to the $P4/mmm$ tetragonal phase of $MAPbCl_3$ and the higher temperature tetragonal (β) phase corresponds to the $I4/mcm$ tetragonal phase of $MAPbI_3$.[20] Khanal and co-workers attributed the formation of either the $P4/mmm$ or $I4/mcm$ tetragonal phase to the B−X bond. In $P4/mmm$, the smaller octahedral volume prevents the free rotation of the MA^+ ions that can occur with larger octahedra in the $I4/mcm$ space group, and thus, $MAPbI_3$ with thelonger Pb−I bond length forms the $I4/mcm$ tetragonal phase while $MAPbCl_3$ with the shorter Pb−Cl bond length forms the $P4/mmm$ tetragonal phase.[33] When $MAPbBr_3$ crystals are subjected to pressure, the volume of the unit cell and the Pb−Br bond length decrease.[34] This results in the disappearance of the $P4/mmm$ (γ) phase at pressures above 43.2 MPa.[21] Chemical doping with Bi causes similar strain, as the effective ionic radius of Bi^{3+} (1.03 Å) is smaller than that of Pb^{2+} (1.19 Å),[35] which should lead to a reduction of the lattice constant and unit cell volume, mimicking the effect of external strain and hence also inducing the disappearance of the $P4/mmm$ (γ) phase. By closely examining the single-crystal XRD data (Figure 3b,c and zoom-in of Figure 1c), we observe that the diffraction plane positions shift to a higher angle, indicating a contraction of the crystal with increasing doping concentration. Notably, we observe such a shift to higher diffraction angles upon doping only when performing XRD on single crystals. For the Bi-doped crystals, after crushing them into powders and performing XRD again, we observe that the diffraction planes return to the same positions as for the undoped crystals (Figure S3), implying that strain builds up in the Bi-doped single crystal and relaxes (possibly to the surface) after grinding. Previous studies also reported that strain exists in Bi-doped $MAPbBr_3$ single crystals, where a broadening of the diffraction peak was observed instead of the shift to a higher angle.[6] That result implies that homogeneous strain existed in their system rather than the dominant compressive strain in our sample series, which might be due to subtle growth differences in the single crystals.

Figure 3a plots the sample phase transition temperatures as a function of the lattice constants extracted from XRD. Here the top and bottom axis are registered following a previous study on undoped $MAPbBr_3$ lattice constants under external pressure.[34] The shift to a lower temperature of the cubic to tetragonal phase transition, as well as the disappearance of two tetragonal phases upon Bi doping, closely resembles the structural effects induced by an external pressure. The tetragonal to orthorhombic phase transition temperature, however, stays relatively unchanged.

Finally, we perform density functional theory (DFT) calculations to examine the effects of the Bi dopant type on the lattice. Bi can be incorporated through a substitution at the

https://dx.doi.org/10.1021/acs.jpclett.1c00334
J. Phys. Chem. Lett. 2021, 12, 2749−2755

Pb site by either Bi^{3+} (Bi_{Pb}^{+}), which donates an electron into the lattice, or an effective Bi^{2+} species that would result in a neutral defect species (Bi_{Pb}^{0}). Hence, we decided to consider two different charge states of Bi on the Pb site. Figure 4a shows the optimized supercell and octahedral structures. The calculated volume of the $[BiBr_6]^{3-}$ (Bi_{Pb}^{+}) octahedron is 10% smaller than that of the $[PbBr_6]^{4-}$ octahedron in the $MAPbBr_3$ lattice, while the $[BiBr_6]^{4-}$ (Bi_{Pb}^{0}) octahedron has a similar volume as the $[PbBr_6]^{4-}$. This indicates that the shorter length of the Bi−Br bond compared with the Pb−Br bond can induce the lattice shrinkage. Since it is computationally demanding to model dilute defect concentration within the DFT framework, we employed a 2 × 2 × 2 supercell of cubic $MAPbBr_3$ that contains 96 atoms and adopted the thermodynamic model of defect pressure.[36] On the basis of the model, we calculated the change in the lattice spacing (a_d) as a function of the Bi_{Pb}^{+} and Bi_{Pb}^{0} concentrations following

$$a_d = a_0(1 + nv_d)^{1/3} \quad (1)$$

where a_0 is the lattice constant of the pristine cell, n is the defect concentration (defects/cm^{-3}), and v_d is the volume of the defect ($Å^3$/defect).[36] The defect volume v_d is derived according to

$$v_d = \frac{p_d V_0}{B_0} \quad (2)$$

where V_0 is the volume of the pristine cell (in $Å^3$/atom), B_0 is the bulk modulus (18.18 GPa), and p_d is the defect pressure (in GPa), which is calculated from eq 3:

$$p_d = -\left(\frac{\Delta[E^{defect}(V) - E^{host}(V)]}{\Delta V}\right) \quad (3)$$

in which E^{defect} and E^{host} are the DFT total energies (in eV) of the defective and pristine cells, respectively.

Figure 4b shows the predicted lattice constant as a function of doping concentration. We find that the Bi_{Pb}^{+} dopant type exhibits a negative slope, similar to our experimental results, while the Bi_{Pb}^{0} dopant type suggests an almost invariant (slightly negative) lattice constant. Here we note that the use of a relatively small supercell with a uniform Bi_{Pb} distribution does not take into account gradual strain change near defect sites, which could account for some of the quantitative discrepancy with actual experiment. However, the qualitative trend of lattice compression predicted for increasing Bi_{Pb}^{+} concentration is indeed consistent with the results from experiment. In addition, we note that Bi_{Pb}^{+} could interact with the native negatively charged defects, of which the most probable sites are MA vacancies (V_{MA}^{-}) and bromine interstitials (Br_i^{-}), forming overall neutral-charged defect pairs, i.e., Bi_{Pb}−V_{MA} and Bi_{Pb}−Br_i.[5,9] We find that both V_{MA}^{-} and Br_i^{-} exhibit an increasing formation energy under pressure (Figure S4), which implies that they have positive defect pressure that expands the lattice, i.e., they will mitigate the lattice contraction should there exist any Bi_{Pb}−V_{MA} or Bi_{Pb}−Br_i bound pairs.

The conductivity measurements (Figure 4c) show that the electrical conductivity increases orders of magnitude upon Bi doping, consistent with literature reports.[8,9] This provides circumstantial evidence that Bi_{Pb}^{+} does indeed form as a donor. From the conductivity measurements and previous reports on carrier mobility as a function of Bi doping,[37] we estimate the electron carrier concentration to be ~1×10^{13} cm^{-3}, 2×10^{16} cm^{-3}, and 1×10^{18} cm^{-3} for the undoped, 0.36% bismuth-doped, and 2.0% bismuth-doped samples, respectively. The doping efficiency, as defined by the ratio of the carrier density to the Bi dopant number, is therefore low (0.1−1%), which is a common feature of halide perovskites due to efficient charge compensation mechanisms. When a charged donor is added, the system can respond by either increasing the electron carrier concentration or forming compensating acceptor defects, for example, through methylammonium loss (V_{MA}), lead loss (V_{Pb}), or iodine gain (I_i). These compensating species could be distributed in the crystal or form bound complexes with Bi. The lack of quantitative agreement between the measurements and predictions for the lattice constant changes with Bi_{Pb}^{+} in Figure 4b is likely due to the nature of these compensating species, which are unresolved at present and will be the subject of further investigation.

In summary, we have demonstrated how doping can influence the structure and phase transitions of halide perovskites. We use specific heat capacity measurements to determine the transition temperatures for various levels of Bi-doped $MAPbBr_3$ single crystals. Bi doping alters the phase transition behavior in $MAPbBr_3$ single crystals. Comparing with the effects of external pressure on the phase transition behaviors, we note that they resemble the effects of external pressure. This observation is consistent with the experimentally observed lattice contraction upon bismuth doping. We further compare DFT calculations with experimental data and suggest that a charged bismuth species replace Pb by forming Bi_{Pb}^{+} defects. These results provide new insight into how doping affects both the lattice structure and order in halide perovskites.

■ ASSOCIATED CONTENT

Supporting Information

The Supporting Information is available free of charge at https://pubs.acs.org/doi/10.1021/acs.jpclett.1c00334.

Detailed single-crystal growth, characterizations (XRD, ICP-OES, microcalorimetry, conductivity), and DFT calculations (PDF)

■ AUTHOR INFORMATION

Corresponding Author

David S. Ginger − *Department of Chemistry, University of Washington, Seattle, Washington 98105, United States;* orcid.org/0000-0002-9759-5447; Email: dginger@uw.edu

Authors

Erin Jedlicka − *Department of Chemistry, University of Washington, Seattle, Washington 98105, United States;* orcid.org/0000-0003-2068-3358

Jian Wang − *Department of Chemistry, University of Washington, Seattle, Washington 98105, United States;* orcid.org/0000-0002-4515-9782

Joshua Mutch − *Department of Physics, University of Washington, Seattle, Washington 98105, United States*

Young-Kwang Jung − *Department of Materials and Science Engineering, Yonsei University, Seoul 03722, Korea;* orcid.org/0000-0003-3848-8163

Preston Went − *Department of Physics, University of Washington, Seattle, Washington 98105, United States*

https://dx.doi.org/10.1021/acs.jpclett.1c00334
J. Phys. Chem. Lett. 2021, 12, 2749−2755

Joseph Mohammed − *Department of Chemistry, University of Washington, Seattle, Washington 98105, United States*
Mark Ziffer − *Department of Chemistry, University of Washington, Seattle, Washington 98105, United States;* orcid.org/0000-0003-2324-3876
Rajiv Giridharagopal − *Department of Chemistry, University of Washington, Seattle, Washington 98105, United States;* orcid.org/0000-0001-6076-852X
Aron Walsh − *Department of Materials and Science Engineering, Yonsei University, Seoul 03722, Korea; Department of Materials, Imperial College London, London SW7 2AZ, United Kingdom;* orcid.org/0000-0001-5460-7033
Jiun-Haw Chu − *Department of Physics, University of Washington, Seattle, Washington 98105, United States*

Complete contact information is available at: https://pubs.acs.org/10.1021/acs.jpclett.1c00334

Author Contributions

[⊥]E.J. and J.W. contributed equally to this work.

Notes

The authors declare no competing financial interest.

■ ACKNOWLEDGMENTS

This research was supported primarily by the National Science Foundation (NSF) through the UW Molecular Engineering Materials Center, a Materials Research Science and Engineering Center (DMR-1719797). Part of this work was conducted at the Molecular Analysis Facility, a National Nanotechnology Coordinated Infrastructure site at the University of Washington that is supported in part by the National Science Foundation (Grant NNCI-1542101), the University of Washington, the Molecular Engineering & Science Institute, and the Clean Energy Institute. J.W. acknowledges the funding support from the Washington Research Foundation and Mistletoe Foundation postdoctoral fellowships. This work was also supported by a National Research Foundation of Korea (NRF) grant funded by the Korean Government (MSIT) (2018R1C1B6008728). Via our membership in the UK's HEC Materials Chemistry Consortium, which is funded by the EPSRC (EP/L000202), this work used the ARCHER UK National Supercomputing Service (http://www.archer.ac.uk).

■ REFERENCES

(1) Kim, J. Y.; Lee, J.; Jung, H. S.; Shin, H.; Park, N. High-Efficiency Perovskite Solar Cells. *Chem. Rev.* **2020**, *120*, 7867−7918.
(2) Quan, L. N.; Rand, B. P.; Friend, R. H.; Mhaisalkar, S. G.; Lee, T.; Sargent, E. H. Perovskites for Next-Generation Optical Sources. *Chem. Rev.* **2019**, *119*, 7444−7477.
(3) Chen, J.; Wang, J.; Xu, X.; Li, J.; Song, J.; Lan, S.; Liu, S.; Cai, B.; Han, B.; Precht, J.; Ginger, D. S.; Zeng, H. Efficient and Bright White Light-Emitting Diodes Based on Single-Layer Heterophase Halide Perovskites. *Nat. Photonics* **2021**, *15*, 238−244.
(4) DeQuilettes, D. W.; Frohna, K.; Emin, D.; Kirchartz, T.; Bulovic, V.; Ginger, D. S.; Stranks, S. D. Charge-Carrier Recombination in Halide Perovskites. *Chem. Rev.* **2019**, *119*, 11007−11019.
(5) Manser, J. S.; Christians, J. A.; Kamat, P. V. Intriguing Optoelectronic Properties of Metal Halide Perovskites. *Chem. Rev.* **2016**, *116*, 12956−13008.
(6) Nayak, P. K.; Sendner, M.; Wenger, B.; Wang, Z.; Sharma, K.; Ramadan, A. J.; Lovrinčić, R.; Pucci, A.; Madhu, P. K.; Snaith, H. J. Impact of Bi^{3+} Heterovalent Doping in the Organic-Inorganic Metal Halide Perovskites. *J. Am. Chem. Soc.* **2018**, *140*, 574−577.
(7) Abdelhady, A. L.; Saidaminov, M. I.; Murali, B.; Adinolfi, V.; Voznyy, O.; Katsiev, K.; Alarousu, E.; Comin, R.; DUrsun, I.; Sinatra, L.; Sargent, E. H.; Mohammed, O. F.; Bakr, O. M. Heterovalent Dopant Incorporation for Bandgap and Type Engineering of Perovskite Crystals. *J. Phys. Chem. Lett.* **2016**, *7*, 295−301.
(8) Meng, R.; Wu, G.; Zhou, J.; Zhou, H.; Fang, H.; Loi, M. A.; Zhang, Y. Understanding the Impact of Bismuth Heterovalent Doping on the Structural and Photophysical Properties of $CH_3NH_3PbBr_3$ Halide Perovskite Crystals with Near-IR Photoluminescence. *Chem. - Eur. J.* **2019**, *25*, 5480−5488.
(9) Sun, P.-P.; Kripalani, D. R.; Bai, L.; Zhou, K. Prediction of the Role of Bismuth Dopants in Organic−Inorganic Lead Halide Perovskites on Photoelectric Properties and Photovoltaic Performance. *J. Phys. Chem. C* **2019**, *123*, 12684−12693.
(10) Hu, Y.; Bai, F.; Liu, X.; Ji, Q.; Miao, X.; Qiu, T.; Zhang, S. Bismuth Incorporation Stabilized α-$CsPbI_3$ for Fully Inorganic Perovskite Solar Cells. *ACS Energy Lett.* **2017**, *2*, 2219−2227.
(11) Zhou, Y.; Chen, J.; Bakr, O. M.; Sun, H. Metal-Doped Lead Halide Perovskites: Synthesis, Properties, and Optoelectronic Applications. *Chem. Mater.* **2018**, *30*, 6589−6613.
(12) Bala, A.; Kumar, V. A Study of Eu Doping in Nanolayers of $CsPbBr_3$ Using Ab Initio Calculations to Understand *f*−*f* Transitions in Eu^{3+}-Doped Nanocrystals for Light-Emitting Diodes. *ACS Appl. Nano Mater.* **2020**, *3*, 4437−4444.
(13) Zhou, Y.; Yong, Z.; Zhang, K.; Liu, B.; Wang, Z.; Hou, J.; Fang, Y.; Zhou, Y.; Sun, H.; Song, B. Ultrabroad Photoluminescence and Electroluminescence at New Wavelengths from Doped Organometal Halide Perovskites. *J. Phys. Chem. Lett.* **2016**, *7*, 2735−2741.
(14) Ma, J.; Yin, J.; Chen, Y.; Zhao, Q.; Zhou, Y.; Li, H.; Kuroiwa, Y.; Moriyoshi, C.; Li, Z.; Bakr, O. M.; Mohammed, O. F.; Sun, H. Defect-Triggered Phase Transition in Cesium Lead Halide Perovskite Nanocystals. *ACS Mater. Lett.* **2019**, *1*, 185−191.
(15) Ma, J.; Chen, J.; Yin, J.; Zhang, B.; Zhao, Q.; Kuroiwa, Y.; Moriyoshi, C.; Hu, L.; Bakr, O. M.; Mohammed, O. F.; Sun, H. Doping Induces Structural Phase Transitions in All-Inorganic Lead Halide Perovskite Nanocrystals. *ACS Mater. Lett.* **2020**, *2*, 367−375.
(16) Xie, A.; Nguyen, T. H.; Hettiarachchi, C.; Witkowski, M. E.; Drozdowski, W.; Birowosuto, M. D.; Wang, H.; Dang, C. X-ray Luminescence in Undoped and Bismuth Doped Single Crystal Hybrid Lead Halide Perovskites. *Proc. SPIE* **2019**, *10912*, No. 109121G.
(17) Saidaminov, M. I.; Abdelhady, A. L.; Murali, B.; Alarousu, E.; Burlakov, V. M.; Peng, W.; Dursun, I.; Wang, L.; He, Y.; Maculan, G.; Goriely, A.; Wu, T.; Mohammed, O. F.; Bakr, O. M. High-Quality Bulk Hybrid Perovskite Single Crystals within Minutes by Inverse Temperature Crystallization. *Nat. Commun.* **2015**, *6* (1), 7586.
(18) Nayak, P. K.; Moore, D. T.; Wenger, B.; Nayak, S.; Haghighirad, A. A.; Fineberg, A.; Noel, N. K.; Reid, O. G.; Rumbles, G.; Kukura, P.; Vincent, K. A.; Snaith, H. J. Mechanism for Rapid Growth of Organic−Inorganic Halide Perovskite Crystals. *Nat. Commun.* **2016**, *7*, 13303.
(19) Shi, D.; Adinolfi, V.; Comin, R.; Yuan, M.; Alarousu, E.; Buin, A.; Chen, Y.; Hoogland, S.; Rothenberger, A.; Katsiev, K.; Losovyj, Y.; Zhang, X.; Dowben, P. A.; Mohammed, O. F.; Sargent, E. H.; Bakr, O. M. Low Trap-State Density and Long Carrier Diffusion in Organolead Trihalide Perovskite Single Crystals. *Science* **2015**, *347* (6221), 519−522.
(20) Onoda-Yamamuro, N.; Matsuo, T.; Suga, H. Calormetric and IR Spectroscopic Studies of Phase Transitions in Methylammonium Trihalogenoplumbates (II). *J. Phys. Chem. Solids* **1990**, *51* (12), 1383−1395.
(21) Onoda-Yamamuro, N.; Yamamuro, O.; Matsuo, T.; Suga, H. *p*−*T* Relations of $CH_3NH_3PbX_3$ (X = Cl, Br, I) Crystals. *J. Phys. Chem. Solids* **1992**, *53* (2), 277−281.
(22) Wang, L.; Wang, K.; Zou, B. Pressure-Induced Structural and Optical Properties of Organometal Halide Perovskite-Based Formamidinium Lead Bromide. *J. Phys. Chem. Lett.* **2016**, *7*, 2556−2562.
(23) Hirotsu, S.; Harada, J.; Iizumi, M.; Gesi, K. Structural Phase Transitions in $CsPbBr_3$. *J. Phys. Soc. Jpn.* **1974**, *37* (5), 1393−1398.

(24) Lee, Y.; Mitzi, D. B.; Barnes, P. W.; Vogt, T. Pressure-Induced Phase Transitions and Templating Effect in Three-Dimensional Organic−Inorganic Hybrid Perovskites. *Phys. Rev. B: Condens. Matter Mater. Phys.* **2003**, *68*, No. 020103.
(25) Jaffe, A.; Lin, Y.; Karunadasa, H. I. Halide Perovskite Under Pressure: Accessing New Properties through Lattice Compression. *ACS Energy Lett.* **2017**, *2*, 1549−1555.
(26) Szafrański, M.; Katrusiak, A. Photovoltaic Hybrid Perovskites under Pressure. *J. Phys. Chem. Lett.* **2017**, *8*, 2496−2506.
(27) Jaffe, A.; Lin, Y.; Beavers, C. M.; Voss, J.; Mao, W. L.; Karunadasa, H. I. *CCDC 1446529: Experimental Crystal Structure Determination*, 2016. DOI: 10.5517/ccdc.csd.cc1kk77l.
(28) Wang, J.; Motaharifar, E.; Murthy, L. N. S.; Higgins, M.; Barrera, D.; Daunis, T. B.; Zheng, Y.; Malko, A. V.; Ely, F.; Quevedo-Lopez, M.; Lee, M.; Hsu, J. W. P. Revealing Lattice and Photocarrier Dynamics of High-Quality $MAPbBr_3$ Single Crystals by Far Infrared Reflection and Surface Photovoltage Spectroscopy. *J. Appl. Phys.* **2019**, *125*, 025706.
(29) Kawachi, S.; Atsumi, M.; Saito, N.; Ohashi, N.; Murakami, Y.; Yamaura, J. Structural and Thermal Properties in Formamidinium and Cs-Mixed Lead Halides. *J. Phys. Chem. Lett.* **2019**, *10*, 6967−6972.
(30) Poglitsch, A.; Weber, D. Dynamic Disorder in Methylammoniumtrihalogenoplumbates (II) Observed by Millimeter-Wave Spectroscopy. *J. Chem. Phys.* **1987**, *87*, 6373−6378.
(31) Swainson, I. P.; Hammond, R. P.; Soulliére, C.; Knop, O.; Massa, W. Phase Transitions in the Perovskite Methylammonium Lead Bromide, $CH_3ND_3PbBr_3$. *J. Solid State Chem.* **2003**, *176*, 97−104.
(32) Swainson, I. P.; Tucker, M. G.; Wilson, D. J.; Winkler, B.; Milman, V. Pressure Response of an Organic-Inorganic perovskite: Methylammonium Lead Bromide. *Chem. Mater.* **2007**, *19*, 2401−2405.
(33) Khanal, R.; Ayers, N.; Banerjee, S.; Choudhury, S. Atomic Structure and Electronic Properties of Lead and Tin Based Hybrid Halide Perovskite Surface for Photovoltaic Applications. *AIP Adv.* **2019**, *9*, 085123.
(34) Zhang, R.; Cai, W.; Bi, T.; Zarifi, N.; Terpstra, T.; Zhang, C.; Verdeny, Z. V.; Zurek, E.; Deemyad, S. Effects of Nonhydrostatic Stress on Structural and Optoelectronic Properties of Methylammonium Lead Bromide Perovskite. *J. Phys. Chem. Lett.* **2017**, *8*, 3457−3465.
(35) Shannon, R. D. Revised Effective Ionic Radii and Systematic Studies of Interatomic Distances in Halides and Chalcogenides. *Acta Crystallogr., Sect. A: Cryst. Phys., Diffr., Theor. Gen. Crystallogr.* **1976**, *A32*, 751−767.
(36) Walsh, A.; Sokol, A. A.; Catlow, C. R. A. Free Energy of Defect Formation: Thermodynamics of Anion Frenkel Pairs in Indium Oxide. *Phys. Rev. B: Condens. Matter Mater. Phys.* **2011**, *83*, 224105.
(37) Ulatowski, A. M.; Wright, A. D.; Wenger, B.; Buizza, L. R. V.; Motti, S. G.; Eggimann, H. J.; Savill, K. J.; Borchert, J.; Snaith, H. J.; Johnston, M. B.; Herz, L. M. Charge-Carrier Trapping Dynamics in Bismuth-Doped Thin Films of $MAPbBr_3$ Perovskite. *J. Phys. Chem. Lett.* **2020**, *11*, 3681−3688.

https://dx.doi.org/10.1021/acs.jpclett.1c00334
J. Phys. Chem. Lett. 2021, 12, 2749−2755